Broadband Extinction and Raman Spectroscopy Measurements to Investigate Optical Properties of Soot Particles in Premixed Flames

F.J. Bauer*[1,2], P.A.B. Braeuer[1,2], M.W.R. Wilke[1], S.R. Faderl[1], S.J. Grauer[2,3], and S. Will[1,2]

[1]Lehrstuhl für Technische Thermodynamik, Friedrich-Alexander-Universität (FAU) Erlangen-Nürnberg, Am Weichselgarten 8, Erlangen 91058, Germany

[2]Erlangen Graduate School in Advanced Optical Technologies, FAU Erlangen-Nürnberg, Paul-Gordan-Straße 6, Erlangen 91052, Germany

[3]Department of Mechanical Engineering, Pennsylvania State University, University Park, PA 16802, United States

Abstract

Three well-defined soot samples from laminar premixed McKenna flames are analyzed by broadband *in situ* and *ex situ* extinction measurements and Raman spectroscopy. The extinction measurements are corrected for scattering based on the aggregate size parameters determined from TEM data. The optical band gap is inferred from the absorption spectra via the Tauc method, which is further compared to the Urbach energy resulting from the same data. Neither method yields a significant advantage or disadvantage. Additionally, there was good agreement between the *in situ* and *ex situ* results. Cross-influences of the evaluation strategy, such as constant offsets and the evaluated wavelength range, are discussed. Finally, the results are compared to Raman spectra from the samples to investigate possible correlations between both techniques.

Introduction

The optical properties of soot particles such as the optical band gap E_g, absorption function $E(\tilde{m})$ or dispersion exponent ζ have been widely used to track the evolution of soot maturity in flames [1–3]. Due to a graphitization-like process, the optical properties change throughout the soot evolution process. Knowledge about the maturity of soot particles is beneficial in a variety of applications. For example, young soot is more reactive than more mature forms, which could be leveraged to counteract pollutant emission through early oxidation [4]. Additionally, soot optical properties are key parameters in the context of carbon black nanomaterials being used in devices such as solar cells and semiconductors [5]. In particular, the optical band gap – the major focus of this work – relates to available electronic transitions of a material, which could potentially be engineered such that the resulting carbon black materials might be utilized as extremely cheap substitutes for conventional semiconductors. Determining the band gap of carbon blacks is difficult due to the effects of one's choice of spectral (fitting) range and assumptions about the underlying transition type, as well as device-specific effects.

The present work provides an overview regarding *in situ* and *ex situ* band gap measurements of soot and highlights some of the most influential parameters. Broadband extinction measurements for wavelengths λ from 200 to 2100 nm are presented in well-characterized premixed flat flames. The data are systematically corrected for impacts such as scattering and analyzed with respect to some recent hypotheses concerning the Urbach energy and the impact of thermally excited free electrons on the absorption behavior [6]. To link the observed results from absorption data to the underlying fine-structural arrangement of the particles, Raman spectroscopy measurements of soot sampled from the flames are performed and discussed.

Theory

Optical properties (including the optical band gap) of soot nanoparticles can be determined via broadband extinction measurements, which can either be performed *in situ* in the flame [7–9] or *ex situ* on soot samples extracted from the flame [10, 11]. The attenuation of light, forming the extinction signal, results from the sum of absorbed and scattered photons. For the evaluation of the optical band gap E_g, only the wavelength-dependent absorption signal is relevant, which requires correcting for the scattering contribution to the extinction signal. Light scattering by soot aggregates mainly depends on their size and morphology-related quantities such as the fractal dimension D_f, the radius of gyration R_g, the primary particle diameter d_p and the number N_p of primary particles forming the aggregate, which can be inferred from transmission electron microscopy (TEM) images or elastic light scattering [12, 13]. With knowledge of these quantities, the aggregate's scattering albedo ω_{agg} – defined as the ratio of the scattering σ_{sca} to the extinction signal σ_{ext} – can be calculated as follows [14]

$$\omega_{agg} = \left\{ 1 + \frac{3}{2}\frac{E(\tilde{m})}{F(\tilde{m})} \left(q\,d_p/2\right)^{-3} \left[N_p\,G\left(q\,R_g\right)\right]^{-1} \right\}^{-1}, \tag{1}$$

with the structure factor

$$G(qR_g) = \left(1 + \frac{4}{3D_f} q^2 R_g^2\right)^{-D_f/2} \tag{2}$$

*Corresponding author: florian.fb.bauer@fau.de

and scattering vector $q = 2\pi/\lambda$. As can be taken from Eq. (1), several wavelength-dependent optical properties are required, i.e., the absorption function $E(\tilde{m})$ and scattering function $F(\tilde{m})$. Both result from the complex refractive index with the real and imaginary parts n and k, respectively. For soot particles, a variety of different values for both parameters exist and (as previously mentioned) they may further change with soot maturity. Here, the obstacle arises that the optical properties must be known to correctly determine the optical properties. Throughout this work, recent data by Wan et al. [15] are used to exclusively correct for the scattering contribution, considering this assumption a second-order effect on the inferred quantities of interest.

Measurements of the spectral intensities of a light source with (I_λ) and without passing the absorbing media ($I_{0,\lambda}$) can be used to calculate the absorbance α_λ following the Beer–Lambert Law,

$$\alpha_\lambda \equiv \ln\left(\frac{I_{0,\lambda}}{I_\lambda}\right) = \int_0^L \kappa_\lambda(l)\,\mathrm{d}l. \tag{3}$$

Both spectral intensity signals I_λ and $I_{0,\lambda}$ are typically background-corrected before being used in Eq. (3), as is done in the present work. This is especially relevant for *in situ* measurements of bright flames. The absorbance can also be expressed as the integral of the absorption path length through the absorbing media L and the local spectral absorption coefficient κ_λ. For the premixed flames under investigation, we assume a homogeneous κ_λ field of at each height above burner (HAB) position: an assumption which may be subject to errors [16]. Once the absorption coefficient spectrum has been determined, it can be used to investigate the electronic transitions of the material. A simplified illustration is adopted from [17] and given in Fig. 1.

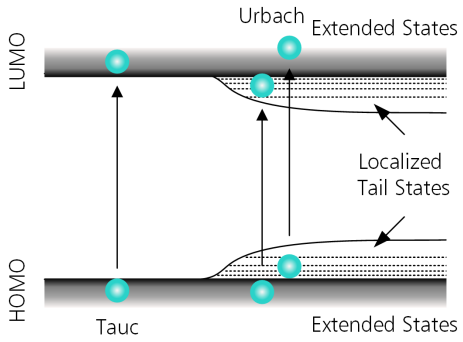

Figure 1: Schematic illustration of transitions between HOMO and LUMO bands, with Tauc and Urbach regions superimposed. Adapted from [17].

The transition between the extended highest occupied molecular orbital (HOMO) state to the extended lowest unoccupied molecular orbital (LUMO) state is called the band gap. It is linked to the absorption coefficient via the proportional relationship introduced by Tauc [18] and Mott and Davis [19],

$$E_\lambda\,\kappa_\lambda \propto \left(E_\lambda - E_\mathrm{g}\right)^k, \tag{4}$$

where h is Planck's constant, $E_\lambda = hc/\lambda$ is the photon's energy and k defines the type of optical transition. In this work, we consider $k = 2$ for an indirect allowed transition based on previous studies [20–23]. However, the exponent can also take a value of 0.5 in case of a direct allowed transition. Following Eq. (4), the band gap can be determined by plotting $(E_\lambda\,\kappa_\lambda)^{1/k}$ versus E_λ and extrapolating a linear fit to the data to the abscissa, with E_g corresponding to the intersection point.

It is well known that soot particles have a complex turbostratic internal structure of polycrystalline graphite layers with defects and dislocations that impact the sp^2 and sp^3 hybridization and ultimately the energetic states. A recent study [6] therefore concluded that, due to the smearing of the sharp energy gaps through the existence of tail states in the forbidden band, the Urbach energy E_U is the better descriptor of the particles' properties. This energy describes an electron transition from an extended state to a tail state or vice versa and appears at lower photon energies compared to the Tauc region. The relationship between the spectrally resolved absorption coefficient and the Urbach energy can be expressed by

$$\kappa_\lambda \propto \exp\left(\frac{E_\lambda}{E_\mathrm{U}}\right). \tag{5}$$

Similar to the Tauc procedure, a linear fit to the data $\ln(\kappa_\lambda)$, plotted against the energy E_λ, allows for extracting the Urbach energy E_U from the inverse slope. The Urbach energy should be inversely proportional to E_g, and as stated in [6], resulting in a high sensitivity to temperature.

It must be mentioned that the determination of E_g and E_U with both techniques is independent of constant factors multiplied by κ_λ, which, e.g., could result from a misinterpretation of the absorption path length or normalization of the spectra. In the case of the Tauc method, a constant multiplied to the data simply impacts the slope of the line but does not affect the intersection point at the x-axis.

The (postulated) high sensitivity of the Urbach energy towards defects in the material can be better interpreted by applying a reference technique to investigate the latter. Raman spectroscopy serves as a valuable tool to study the disorder and defect density of soot samples. Here, soot exhibits two characteristic first-order bands (called D1 and G) and a second-order 2D band. Typically, the measurements are decomposed into individual peaks that are indicative of characteristic internal fine structures. Most importantly, the ratio between D1/G yields insight into the defect density.

Data acquisition and experimental set-up

The investigated soot samples result from laminar premixed flames for which corresponding TEM data are available [12]. The key quantities derived from TEM are summarized in Table 1. *In situ* and *ex situ* measurements were taken in a bronze McKenna burner with the stabilization plate mounted at HAB 26 mm.

The *in situ* setup is shown in Fig. 2. A fiber-

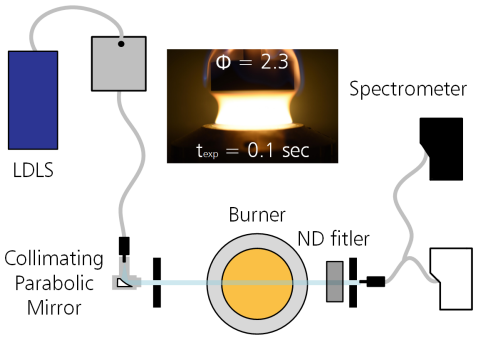

Figure 2: Schematic illustration of the experimental setup used for broadband extinction measurements.

coupled laser-driven light source provides light from 200–2100 nm, which is collimated by an off-axis parabolic UV-enhanced aluminum mirror. The light passes through the flame into a detection split fiber, which is connected to two spectrometers covering different spectral ranges. For measurements in a spectral range from 300 to 1000 nm, a QEPro spectrometer (Ocean Insight) is used, and from 1000 to 2200 nm, a NIRQuest spectrometer (Ocean Insight) was utilized. To avoid overexposure, an additional neutral density filter with an optical density of OD2 is placed in front of the detection fiber. For *in situ* measurements, an OFX (Ocean Insight) spectrometer with a solarization-resistant detection fiber is used to cover the range from 200 to 300 nm in a sequential recording. Two apertures are mounted: first after the collimating mirror and second at the entrance of the detection fiber to allow for spatial sampling from the beam of light.

For *ex situ* measurements, the soot was extracted from the flame by rapid insertion of microscopy coverslip plates with a loading time of approximately 500 ms – similar to those used by [10, 11]. The samples were investigated with the setup shown in Fig. 2 by placing the plates with the soot samples in the beam of light.

Raman measurements were performed on the soot samples following the procedure described in [20]. However, measurements reported here were conducted with a 532 nm continuous wave laser and a spectrometer (Ocean Insight, QE65000) with 1200 grooves/mm.

Results and discussion

Both the *in situ* and *ex situ* extinction measurements in the premixed flames are depicted in Fig. 3. With knowledge about the absorption path length (which equals the flame diameter), the *in situ* data can be evaluated quantitatively, following Eq. (3). In the case of the *ex situ* samples, the absorption path length, resulting from the loading efficiency of soot particles on the coverslip plate, is more difficult to quantify. To facilitate a comparison between *in situ* and *ex situ* measurements, the latter were first normalized to the maximum value and then multiplied by a factor of the according *in situ* data. It should be repeated that a constant normalization value does not affect the following Tauc or Urbach energy procedure.

Table 1: Premixed flames and corresponding mean TEM parameters from [12].

Fuel	Φ	**HAB,** mm	$\bar{d}_\mathrm{p}$, nm	$\bar{N}_\mathrm{p}$	$\bar{R}_\mathrm{g}$, nm	$\bar{D}_\mathrm{f}$
C_2H_2	2.3	17	20.2	74.1	77.0	1.60
	2.7	17	25.7	143.5	132.8	1.62
C_2H_4	2.7	17	30.2	35.7	75.2	1.62

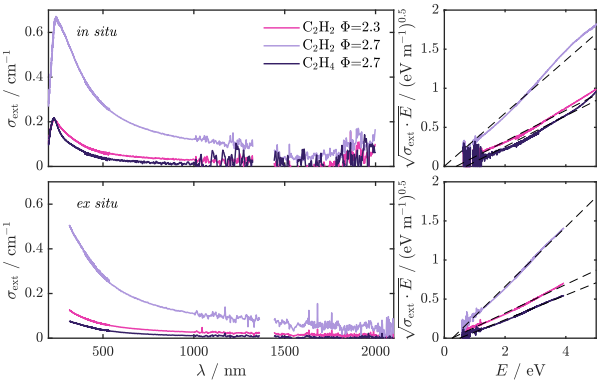

Figure 3: Top: *In situ* extinction spectra taken in 3 flames with resulting Tauc plots on the right side. Bottom: *Ex situ* measurements normalized and scaled to the *in situ* measurements for the corresponding samples.

The spectra reveal that the fuel C_2H_2 results in increased extinction compared to C_2H_4 and that the light extinction increases with increasing equivalence ratio Φ. The gap at approximately 1400 nm results from the transmission characteristics of the detection fiber. Additionally, for the *in situ* measurements an increased absorption can be observed towards 2000 nm, which results from hot H_2O absorption as a major combustion product in the flame. Next to the extinction measurements on the right side the resulting Tauc plots are shown with linear fits to the entire spectral range. While the *ex situ* data reveal a more or less linear behavior, the *in situ* data show stronger discrepancies at the high energy regions >3.5 eV, which most likely result from absorption of polycyclic aromatic hydrocarbons (PAHs) in the flame. The *ex situ* measurements are limited in the UV by the absorption of the coverslip glass.

In a next step, for the three soot samples with their size parameters listed in Table 1 the scattering albedos are calculated following Eq. (1) and Eq. (2). The results are shown in Fig. 4 with the same color coding as used in Fig. 3.

As can be seen, the scattering contribution increases towards the UV and is stronger for large aggregates in the C_2H_2 $\Phi = 2.7$ case (purple line) compared to larger primary particles in the C_2H_4 $\Phi = 2.7$ data (dark violet line). The extinction spectra can now be corrected for the scattering contribution resulting in the absorp-

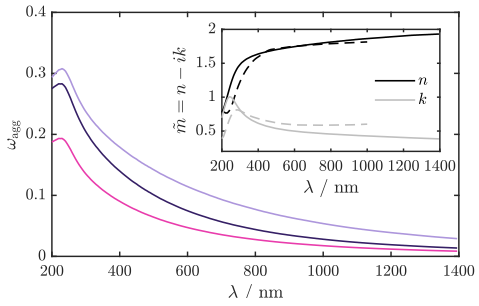

Figure 4: Calculated scattering albedo following Eq. (1) and Eq. (2) for aggregates as listed in Table 1 with the complex refractive index m taken from Wan et al. [15]. For latter, both parameters n and k are shown as solid lines in the inset with a comparison to older data from Chang and Charalampopoulos [24] depicted as dashed lines.

tion spectra, which are given with the according Tauc plots in Fig. 5.

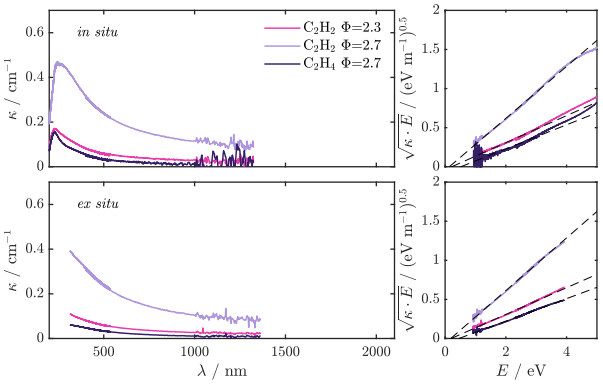

Figure 5: Top: *In situ* absorption spectra taken in 3 flames with resulting Tauc plots on the right side. Bottom: *Ex situ* measurements normalized and scaled to the *in situ* measurements for the corresponding samples.

As data on n and k from [15] are limited from 200 to 1400 nm, the upcoming evaluations are restricted to this region. It should be noted, however, that the spectra in Fig. 3 have a more or less continuous trend towards the longer wavelengths and no pronounced bending of the spectra is evident that would be indicative of the Urbach tail. Table 2 summarizes the resulting optical band gaps from the *ex situ* and *in situ* Tauc analysis for a linear fit to the data at an energy range from 0.9 to 3.5 eV. There is a discrepancy of up to 0.07 eV between *in situ* and *ex situ* measurements.

Additionally, the impact of the scattering correction should be investigated by evaluating the same energy range for the κ_λ and σ_{ext} spectra of Fig. 5 and Fig. 3, respectively. Neglecting the scattering share results in an overestimation of E_g by 0.07 eV in the C_2H_4 $\Phi = 2.7$ as well as the C_2H_2 $\Phi = 2.3$ case and up to 0.13 eV in the C_2H_2 $\Phi = 2.7$ case. Readers should recall that the huge aggregates of the latter soot sample reflect a kind of worst-case-scenario.

Another important influence is a constant offset (equal for each wavelength) superimposed to the spectra, which might result from intensity variations of the light source between I_λ and $I_{0,\lambda}$ recording, stray light impacts in the detection device, or reflections due to misplacement of the sampling substrate in case of *ex situ* measurements. Adding a simulated offset of +5% of the mean κ value to the absorption spectrum results in a band gap bias of -0.06 eV and +0.06 eV if 5% are subtracted.

As addressed in multiple studies, a strong dependency on the evaluated wavelength range can be expected. Therefore, in a next step a case study with varying spectral ranges was performed on the example of *in situ* absorption data at C_2H_2 $\Phi = 2.7$. The resulting Tauc plot is shown on top of Fig. 6.

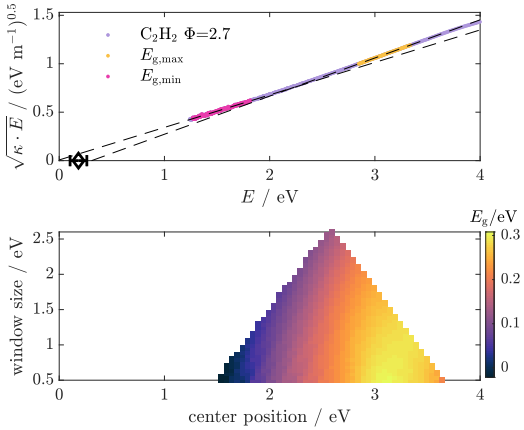

Figure 6: Impact of the evaluated wavelength range on the inferred optical band gap value. The upper plot shows the underlying data with the fits resulting in minimal and maximal E_g. The lower plot shows the variation of window size vs. central wavelength position.

Below, a plot of the resulting band gap values in different colors is shown by varying the center positions and the window size of the evaluated energy range. A straight vertical line from the tip of the triangle to the base therefore corresponds to a symmetrically increasing width of the energy range around the center value of 2.6 eV. The plot reveals that the choice of the center value is more important than the width with decreasing values towards the lower energies and therefore infrared wavelength regions. The two extreme examples differ

Table 2: Resulting optical band gaps and Urbach energies for various cases of the soot samples each taken at HAB=17 mm.

Fuel	Φ	E_g, eV *ex situ*	E_g eV *in situ*	E_U, eV *ex situ*	E_U eV *in situ*	D1/G
C_2H_2	2.3	0.20	0.22	1.79	1.81	2.62
	2.7	0.18	0.14	1.83	1.91	2.47
C_2H_4	2.7	0.45	0.52	1.38	1.19	3.12

by a value of approximately 0.3 eV and are marked in the upper Tauc plot with orange and magenta colored data points. The large difference of the inferred band gap value regarding different energy ranges described in previous work [6] of up to 1.3 eV could not be confirmed.

Next, the absorption spectra are interpreted utilizing the Urbach approach. Figure 7 shows the Urbach plots for the three *in situ* and *ex situ* samples, which were first normalized to facilitate comparison. From the inverse slope, the Urbach energies can be inferred and the results are given in Table 2 for an evaluated energy range between 1.3 to 3.5 eV depicted as dashed vertical lines.

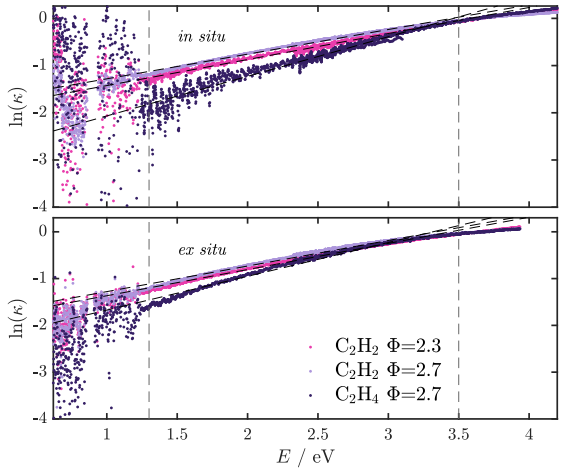

Figure 7: Urbach plot following Eq. (5) for the 3 scattering corrected absorption data with the linear fits in an energy range from 1.3 to 3.5 eV.

This evaluation range is based on the choice of [6], while in our case the lower energy limit could be extended down to 1.3 eV without noise restrictions. However, no clear linear trend is observable resulting in similar or even more pronounced dependencies of E_U on the evaluated energy range as for the Tauc procedure. The inverse correlation between E_U and E_g is given, however, no pronounced difference between *ex situ* and *in situ* measurements could be observed. The Urbach energies overall decrease by shifting the evaluation range to lower energies or longer wavelengths.

Figure 8 shows the Raman spectra of the samples, with the spectrum of C_2H_2 $\Phi = 2.3$ decomposed into five Voigt profiles following [25, 26]. For the three samples, the D1/G ratio is given in Table 2. A direct proportionality to the E_g values can be observed, which might be indicative of a crystallite size of $L_a > 2$ nm [27]. In this case, higher D1/G values correlate with higher defect densities. This confirms the finding that C_2H_2 soot is more graphitized than C_2H_4 soot [28].

Conclusions

Flame temperatures present during *in situ* measurements do not strongly impact the optical band gap nor the Urbach energy in comparison to *ex situ* measurements, confirming the results by Russo et al. [9]. The observed differences might mainly result from the simultaneous presence of other combustion species such as H_2O or PAHs. However, qualitative trends between *ex situ* and *in situ* measurements of E_g agree, making the latter a valuable tool to track soot maturity in flames. The (very) broadband measurements of the present work enabled a detailed study on the impact of the evaluated wavelength range on estimates of E_g. Here, a strong dependency was found leading to the conclusion that caution is required when attributing a certain value of E_g to the measurements. At the same time, the measured data can neither be correctly explained by the Tauc nor the Urbach procedure (requiring linear trends), which leads to the fact that neither procedures is preferable. Careful attention should be paid to device-specific impacts such as stray light or nonlinear behavior to avoid biased results.

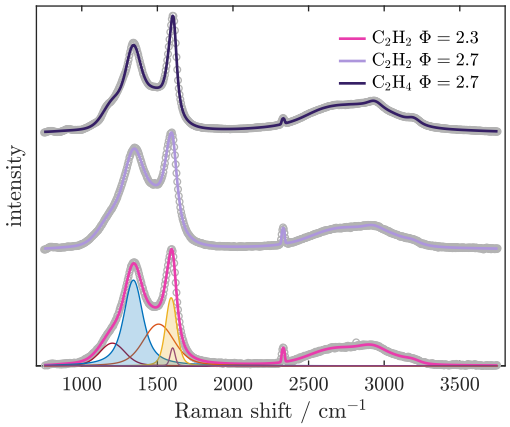

Figure 8: Raman specta of the samples with spectral decomposition following [25, 26]. The D1 and G peak are depicted as filled peaks in blue and yellow, respectively.

Acknowledgments

The authors gratefully acknowledge funding of the Erlangen Graduate School in Advanced Optical Technologies (SAOT) by the Bavarian State Ministry for Science and Art.

References

[1] J. Yon, J. J. Cruz, F. Escudero, J. Morán, F. Liu, and A. Fuentes, Revealing soot maturity based on multi-wavelength absorption/emission measurements in laminar axisymmetric coflow ethylene diffusion flames, *Combust. Flame* **227**, 147 (2021).

[2] G. A. Kelesidis, C. A. Bruun, and S. E. Pratsinis, The impact of organic carbon on soot light absorption, *Carbon* **172**, 742 (2021).

[3] B. Ma and M. B. Long, Combined soot optical characterization using 2-D multi-angle light scattering and spectrally resolved line-of-sight attenuation and its implication on soot color-ratio py-

rometry, *Appl. Phys. B* **117**, 287 (2014).

[4] F. P. Hagen, D. Kretzler, T. Häber, H. Bockhorn, R. Suntz, and D. Trimis, Carbon nanostructure and reactivity of soot particles from non-intrusive methods based on uv-vis spectroscopy and time-resolved laser-induced incandescence, *Carbon* **182**, 634 (2021).

[5] S. Khodabakhshi, P. F. Fulvio, and E. Andreoli, Carbon black reborn: Structure and chemistry for renewable energy harnessing, *Carbon* **162**, 604 (2020).

[6] F. Migliorini, S. Belmuso, R. Dondè, S. De Iuliis, and I. Altman, To optical properties of carbon nanoparticles: A need in comprehending Urbach energy, *Carbon Trends* **8**, 100184 (2022).

[7] P. Minutolo, G. Gambi, and A. D'Alessio, The optical band gap model in the interpretation of the UV-visible absorption spectra of rich premixed flames, *Symp. (Int.) Combust.* **26**, 951 (1996).

[8] E. M. Adkins and J. H. Miller, Extinction measurements for optical band gap determination of soot in a series of nitrogen-diluted ethylene/air non-premixed flames, *Phys. Chem. Chem. Phys.* **17**, 2686 (2015).

[9] C. Russo, B. Apicella, A. Tregrossi, A. Ciajolo, K. C. Le, S. Török, and P.-E. Bengtsson, Optical band gap analysis of soot and organic carbon in premixed ethylene flames: Comparison of in-situ and ex-situ absorption measurements, *Carbon* **158**, 89 (2020).

[10] A. Tregrossi and A. Ciajolo, Spectral signatures of carbon particulate evolution in methane flames, *Combust. Sci. Technol.* **182**, 683 (2010).

[11] C. Russo, F. Stanzione, A. Ciajolo, and A. Tregrossi, Study on the contribution of different molecular weight species to the absorption UV–Visible spectra of flame-formed carbon species, *Proc. Combust. Inst.* **34**, 3661 (2013).

[12] M. Altenhoff, S. Aßmann, C. Teige, F. J. Huber, and S. Will, An optimized evaluation strategy for a comprehensive morphological soot nanoparticle aggregate characterization by electron microscopy, *J. Aerosol Sci.* **139**, 105470 (2020).

[13] H. Oltmann, J. Reimann, and S. Will, Wide-angle light scattering (WALS) for soot aggregate characterization, *Combust. Flame* **157**, 516 (2010).

[14] C. Sorensen, Light scattering by fractal aggregates: a review, *Aerosol Sci. Technol.* **35**, 648 (2001).

[15] K. Wan, X. Shi, and H. Wang, Quantum confinement and size resolved modeling of electronic and optical properties of small soot particles, *Proc. Combust. Inst.* **38**, 1517 (2021).

[16] F. Migliorini, S. De Iuliis, F. Cignoli, and G. Zizak, How "flat" is the rich premixed flame produced by your McKenna burner?, *Combust. Flame* **153**, 384 (2008).

[17] N. Sharma, K. Prabakar, S. Ilango, S. Dash, and A. Tyagi, Optical band-gap and associated Urbach energy tails in defected AlN thin films grown by ion beam sputter deposition: Effect of assisted ion energy, *Adv. Mater. Proc.* **2**, 342 (2017).

[18] J. Tauc, R. Grigorovici, and A. Vancu, Optical properties and electronic structure of amorphous germanium, *Phys. Status Solidi B* **15**, 627 (1966).

[19] N. F. Mott and E. A. Davis, *Electronic Processes in Non-crystalline Materials* (Oxford University Press, 2012), 2nd ed.

[20] F. J. Bauer, P. A. Braeuer, S. Aßmann, M. A. Thiele, F. J. Huber, and S. Will, Characterisation of the transition type in optical band gap analysis of in-flame soot, *Combust. Flame* **243**, 111986 (2022).

[21] C. Liu, A. V. Singh, C. Saggese, Q. Tang, D. Chen, K. Wan, M. Vinciguerra, M. Commodo, G. D. Falco, P. Minutolo, et al., Flame-formed carbon nanoparticles exhibit quantum dot behaviors, *Proc. Natl. Acad. Sci.* **116**, 12692 (2019).

[22] D. Chen and H. Wang, HOMO–LUMO gaps of homogeneous polycyclic aromatic hydrocarbon clusters, *J. Phys. Chem. C* **123**, 27785 (2019).

[23] G. De Falco, G. Mattiello, M. Commodo, P. Minutolo, X. Shi, A. D'Anna, and H. Wang, Electronic band gap of flame-formed carbon nanoparticles by scanning tunneling spectroscopy, *Proc. Combust. Inst.* **38**, 1805 (2021).

[24] H.-c. Chang and T. Charalampopoulos, Determination of the wavelength dependence of refractive indices of flame soot, *Proceedings of the Royal Society of London. Series A: Mathematical and Physical Sciences* **430**, 577 (1990).

[25] A. Sadezky, H. Muckenhuber, H. Grothe, R. Niessner, and U. Pöschl, Raman microspectroscopy of soot and related carbonaceous materials: Spectral analysis and structural information, *Carbon* **43**, 1731 (2005).

[26] P. A. Braeuer, L. A. Bahr, H.-J. Koß, and S. Will, Advanced spectral reconstruction (ASR) for setup-independent universal Raman spectroscopy models, *Chemom. Intell. Lab. Syst.* **232**, 104730 (2023).

[27] J. D. Herdman, B. C. Connelly, M. D. Smooke, M. B. Long, and J. H. Miller, A comparison of raman signatures and laser-induced incandescence with direct numerical simulation of soot growth in non-premixed ethylene/air flames, *Carbon* **49**, 5298 (2011).

[28] A. Drakon, A. Eremin, E. Gurentsov, E. Y. Mikheyeva, and R. Kolotushkin, Optical properties and structure of acetylene flame soot, *Applied Physics B* **127**, 81 (2021).